In-situ high-pressure transmission electron microscopy for earth and materials sciences

JUN WU and PETER R. BUSECK

School of Earth and Space Exploration and Department of Chemistry and Biochemistry, Arizona State University, Tempe, AZ 85287, U.S.A.

REVISION 1

ABSTRACT

Transmission electron microscopy in combination with in-situ high-pressure and high-temperature measurements is uniquely able to provide high-resolution data about materials under conditions resembling those in Earth's interior. By using nanocontainers made of graphitized carbon, it is possible to achieve pressures and temperatures up to at least 40 GPa and 1500 °C, respectively. A wide range of relatively simple minerals have been studied using this approach. Results to date show the influence of crystallographic defects in concentrating and storing carbon within analogs to minerals occurring deep inside Earth.

Keywords: in-situ transmission electron microscopy, high-pressure measurements, carbon nanocontainers, carbon nanotubes (CNTs), carbon nanofibers (CNFs), carbon nano-onions (CNOs)

INTRODUCTION

Transmission electron microscopy (TEM) has long been used to study the products of high-pressure experiments at the near-atomic scale. However, in all cases it has been necessary to quench the samples before they could be imaged at high resolution (Mao and Hemley 1998). Diamond-anvil cells (DACs) and multi-anvil presses (MAPs), the instruments currently used for pressure generation, prevent the *in-situ* use of TEM because their substantial sizes preclude the necessary electron transparency. As a consequence, in-situ TEM applications for experiments at gigapascal pressure ranges, particularly meaningful to the earth sciences, have been impossible up to now.

X-ray diffraction and other spectroscopic techniques available for in-situ high-pressure research acquire statistical information averaged over the relatively large sample volumes interacting with the source radiation. However, in many cases, studies of crystal defects and mineral reactions at unit-cell dimensions are central to understanding geophysics and geochemistry in Earth's interior (Cordier 2002; Karato 2010; Stixrude and Lithgow-Bertelloni 2012). TEM is one of the most useful techniques,

and commonly the only one, for observing defect features and analyzing chemical compositions at down to atomic resolutions (Buseck 1992; Veblen 1985). Therefore, in-situ TEM capabilities at high pressure have long been desired within the earth and materials science communities.

The goal of this paper is to provide an overview of recent efforts to develop and refine an in-situ, high-pressure TEM method for the earth and materials sciences. With successful applications to geophysically significant minerals and mineral analogs, we demonstrate the feasibility and potential of this new technique.

GRAPHITIC NANOCONTAINERS AND NANOPRESSES

Graphitic networks can lose carbon atoms through displacement damage and vacancy formation when exposed to electrons with acceleration voltages over ~86 kV in an electron microscope (Smith and Luzzi 2001). If the graphitic networks are curved on the nanometer scale and the temperature is raised to above ~300 °C, structural reorganization occurs around the relatively immobile vacancies in the networks, causing their shrinkage (Fig. 1) (Banhart 1999; Banhart 2004; Krasheninnikov et al. 2005). If they are in the form of closed containers that enclose condensed materials, compression of the enclosed materials occurs (Banhart and Ajayan 1996). Calculations indicate that if the containers are sufficiently small, what we call nanocontainers, then

the internal pressures can reach 40 GPa in, for example, multi-walled carbon nanotubes (CNTs) (Sun et al. 2006a).

Pressure generation in carbon containers can be understood in terms of Laplace's law, which relates internal pressure (P) of a fluid-filled hollow vessel to wall tension (T) and its hollow radius (R). For a cylindrical vessel, $T = P \cdot R$, whereas $T = P \cdot R/2$ for a spherical vessel. The wall tension of a 19-shelled CNT is at least 140 N/m (Sun et al. 2006b). Atomistic calculations suggest that internal pressures in multi-walled CNTs converge to a maximum with only ~6 graphitic shells, such that further increases in the number of walls do not produce proportional pressure increases (Sun et al. 2006a). Therefore, for an inner sample diameter of 100 nm, the electron-transparent thickness limit for most materials, maximum internal pressures of greater than 2.8 and 5.6 GPa would be expected in tubular and spherical graphitic containers, respectively.

The workable wall thicknesses are limited by half of the mean absorption distance (λ) for graphite since the container walls both below and above an enclosed sample interact with the incident electrons. For a typical TEM acceleration voltage and collection angle, e.g., 300 kV and 3 mrad, respectively, λ is ~225 nm (Akhtar et al. 2012).

Carbon nanocontainers enclosing samples of interest can be prepared through either insertion of samples into pre-existing containers or growth around the minerals of interest. If sufficiently thin, the walls of these carbon nanocontainers permit the use of standard TEM techniques that include selected-area electron diffraction (SAED),

convergent-beam electron diffraction (CBED), high-resolution TEM (HRTEM), energy-dispersive X-ray spectroscopy (EDS), electron energy-loss spectroscopy (EELS), and energy-filtered TEM (EFTEM).

METHOD DESCRIPTION

Growing suitable containers

Carbon nanocontainers are essential for TEM measurements at elevated pressures. The containers can be: (a) CNTs consisting of rolls of graphene layers that form hollow tubes (Fig. 2a), (b) carbon nanofibers (CNFs) that consist of graphene layers arranged as stacked cones or cups (Fig. 2b), (c) carbon nano-onions (CNOs) that are spherical and made of multiple graphene layers surrounding an empty core (Fig. 2c), or (d) poorly graphitic cages or hydrocarbon coatings that can be graphitized under controlled conditions within the column of the electron microscope. In all cases, the containers should be as perfectly graphitized as possible prior to starting the high-pressure experiments. CNTs, CNFs, and CNOs are available commercially but can also be readily synthesized in laboratories by using arc discharge, chemical vapor deposition (CVD), or laser ablation (Fig. 3).

Loading minerals into carbon nanocontainers

Placing minerals of interest into tiny carbon containers is a major challenge. We used two approaches: (a) filling existing containers, and (b) growing the containers around

96 nanoparticles of interest. For convenience, we call them type-A and type-B containers,
97 respectively.

98 Type-A containers are tubular CNTs or CNFs and can be loaded through capillary
99 introduction of solutions or melts from which the solids of interest crystallize (Dujardin
100 et al. 1994). The fluids can be of mineral samples or their precursors, either in the
101 molten state or in solution, commonly followed by thermal decomposition (Ajayan and
102 Iijima 1993; Tsang et al. 1994). This method has proven particularly useful for loading
103 oxide minerals such as magnetite (Fe_3O_4), shcherbinaite (V_2O_5), and bunsenite (NiO)
104 (Fig. 4). A typical loading yield is at least 1% of all containers in the product. Improving
105 the loading efficiency remains an area of study.

106 A challenge with using type-A containers is that they typically form with closed
107 ends and therefore must be opened prior to sample insertion. The containers can be
108 opened mechanically through milling or chemically by oxidizing agents such as hot
109 solutions of HNO_3 or other acids or by air at high temperature. If desired, the open ends
110 of a container containing a sample can be closed by intentionally irradiating the ends
111 (Ugarte, 1992).

112 Silicates are important for high-pressure geoscience studies but are difficult to put
113 into nanocontainers. Specific procedures are needed for different minerals. Here we
114 illustrate the use of olivine, for which capillary wetting works well for the type-A
115 containers (Fig. 5). To fill CNFs with single-crystal olivine, we immersed open CNFs

into a sol created by mixing tetraethyl orthosilicate ($Si(OC_2H_5)_4$), magnesian nitrate hexahydrate ($Mg(NO_3)_2{\cdot}6H_2O$), and 1-M nitric acid (HNO_3) in a mass ratio of 1:2.4:36 (Sanosh et al. 2010). The mixture was stirred for 12 hours, followed by programmed annealing of the CNFs sifted from the solution.

An alternate approach to filling CNFs (or CNTs) is to deposit graphitic layers directly onto nanosized mineral grains, thereby creating nanocontainers. The resulting type-B containers tightly encapsulate nanoparticles of interest when the latter are suspended freely in or passed through an atmosphere containing carbon vapor. It also seems that coating can occur when the particles move on the substrate, presumably because of thermal vibration. An advantage of the coating approach is that it avoids formation of defects during opening the closed type-A containers.

Type-B containers can be produced by the methods illustrated in Figure 3, of which CVD and laser ablation have been the most useful. To coat nanoparticles with graphitic carbon we either dispersed them onto TEM grids, which were then placed into the hot zone of a tube furnace, or we suspended the nanoparticles in a flowing inert gas, which transported them through the hot zone of the furnace.

When employing the arc-discharge method, a graphite rod impregnated with a target material or its components is used as an electrode. Carbon nanocontainers filled with the target material form in the discharge product. For example, we used a silicon-impregnated graphite rod in an arc and obtained moissanite (SiC)-filled CNOs. A

limitation of this procedure is that the target materials have to be stable under the high temperature (up to 3500 °C) and reducing carbon atmosphere in an arc.

Another way to create type-B containers is to take advantage of the fact that amorphous or poorly graphitic carbon is graphitized under electron radiation (Ugarte 1992). Also, CVD, laser ablation, and arc discharge can all grow amorphous and poorly graphitic carbon within their reaction regions if the temperature is lower than ~600 °C. Yet one more convenient way to deposit amorphous carbon is to dip nanocrystals into an organic solvent such as acetone and then decompose this coating under electron radiation (Wu and Buseck 2013).

The preferable choice of method for loading minerals into carbon nanocontainers depends on the sample. Table 1 summarizes our sample-loading methods used to date and the minerals that have been loaded successfully.

Achieving high temperatures plus thermal and mechanical stability within an electron microscope

Sample heating to above ~300 °C is necessary for shrinking carbon nanocontainers during electron irradiation. At elevated temperatures, displaced carbon interstitials are sufficiently mobile to prevent their clustering and thus losing their ability to recombine with vacancies. As a result, self-rearrangement of the atomic structure around vacancies leading to shrinkage of these containers can occur. On the other hand, because of limited direct exposure to electrons of samples plus their good contact with conductive

carbon container walls, sample heating through electron radiation results in only small temperature changes. Using data from Williams and Carter (1996), the temperature changes are estimated to be <10 °C in our experiments.

Controlling sample temperature is important for high-pressure research. It is far easier to precisely control heating (up to 1500 °C) within an electron microscope than in high-pressure instruments such as MAPs and DACs. However, maintaining positional stability during rapid sample heating and cooling is both necessary and difficult for reliable TEM measurements. This concern arises because sample drift and stage vibration when changing the temperature can degrade high-resolution imaging and effectively inhibit TEM examination.

Controlling mechanical stability is especially problematic when using standard furnace-type TEM heating holders. The recent development of heating holders that utilize a MEMS (micro-electro-mechanical systems) design provides a good solution. Significantly improved sample stability and heating rate relative to standard stages can be achieved in this way (Fig. 6). More remarkably, even a substantial temperature increase of 300 °C caused no significant sample drift so that no sample translation was needed to record the image at 400 kX. Therefore, it is possible to capture features at atomic resolution in the sample without concern about instability-induced resolution loss. A MEMS holder also allows in-situ EDS analyses with a windowed detector at

175 temperatures up to ~800 °C, which is difficult or impossible with standard furnace-type
176 holders.

177 **Compressing minerals through electron irradiation**

178 The rate of pressure increase during electron irradiation depends on the current
179 density of the electron beam. Because electrons have a small mass, their displacement
180 ability is relatively weak, with a cross section of 180 barn for interaction at 100 kV with
181 carbon atoms (Cosslett 1978). As a result, electron-induced vacancy creation in the
182 graphitic networks is slow, as is the pressure buildup. We used electron beams with
183 current densities on the order of 10-100 A/cm^2 and irradiation durations of tens to
184 hundreds of minutes.

185 Using such energetic electrons, radiation damage to the enclosed mineral samples
186 can be a problem, especially for beam-sensitive silicates. One way to mitigate this
187 situation is to minimize sample exposure to the electron beam. We achieved this goal by
188 using the condenser-lens stigmators of the microscope to distort the electron beam into
189 an elongated shape that was positioned along the walls of the carbon nanocontainer
190 adjacent to the enclosed sample. An alternate way to achieve the same goal is to use a
191 nanoprobe in STEM mode and then raster the beam along the walls along a pre-defined
192 path under software control.

193 Figure 7 illustrates a forsterite nanocrystal that was compressed in a shrinking CNF.
194 By comparing diffraction patterns recorded before and after compression, a ~3.8%

radial strain was measured in the nanocrystal. In light of its unknown crystallographic orientation, we approximate the Young's modulus and Poisson's ratio to those (~200 GPa and ~0.24, respectively) for polycrystalline forsterite. The generalized Hooke's law then yields a radial pressure of ~10 GPa in the forsterite.

Whether the compression is hydrostatic or not depends on the morphology of the carbon nanocontainers. Shrinking tubular nanocontainers (CNTs and CNFs) provides non-uniform compression, whereas spherical containers (CNOs) generate relatively hydrostatic pressures. Both hydrostatic and directional (deviatoric) stresses can be useful experimentally, depending on the problem being addressed.

Measuring pressures

As with many high-pressure studies, we used the equation of state (EoS) of the crystalline samples to estimate the pressure they experienced. Pressure-induced decreases in lattice spacings appear as increases in the distances of the relevant reciprocal spots from the central spot in either diffraction patterns or diffractograms derived from fast Fourier transforms (FFT) of HRTEM images (Fig. 8). The volume change estimated from the change in sample lattice spacing was then used in the Birch-Murnaghan EoS to calculate the pressure. Plots of pressure versus time or incident electron current density can also be attained by measuring temporal changes in lattice spacing at different beam current densities.

Uncertainties in pressure estimates using SAED patterns or FFT-derived diffractograms are dominated by systematic errors generated when comparing lattice spacings before and after compression. When the comparison is done for identical experimental conditions except pressure, the errors arise primarily from the finite sizes of the nanocrystal and CCD pixels. For the zincite case (Fig. 8), we estimate a ~16% uncertainty in the measurement of the lattice-spacing decrease, which corresponds to a ~20% uncertainty in the pressure estimate of ~18 GPa. An improved way of measuring internal pressure that we plan to explore is to take advantage of pressure-dependent features in electron-generated spectra such as cathodoluminescence from the sample under compression.

Observing minerals in situ under pressure

Observation of pressurized mineral samples is the same as for TEM examination of materials at ambient conditions, i.e., high-resolution imaging and chemical analyses can be readily done while the pressure and temperature are maintained. More important, direct observation of defects and real-time TEM of phase transitions at elevated pressures become possible for the earth sciences for the first time. For example, Figure 9 shows the real-time monitoring of anatase to α-PbO_2-type structure and concordant development of an associated stacking fault in titanium dioxide at >8 GPa and 770 °C.

High-pressure study of samples at low temperatures is also possible by cooling the

233 samples after a desired internal pressure is reached. A subsequent temperature change
234 would have only a slight effect on the internal pressure maintained inside the
235 containers. However, inevitable agglomeration of radiation-induced defects at low
236 temperatures will lead to structural disorder in the container walls at a rate that
237 depends on the incident beam current density, and this disorder causes a gradual
238 relaxation in the internal pressure. Therefore, a relatively low electron dose is suggested
239 for such TEM observations at low temperatures.

240 Despite its power, this technique also has limitations. The small sizes of the carbon
241 containers, as well as the sample-thickness limit imposed by TEM, make it difficult to
242 apply the technique to studies of coarse-grained samples. Also, high-pressure
243 properties of nano-sized samples measured using this method may not represent those
244 of their bulk counterparts, and possible modifications of the samples might occur
245 because of the affinity of displaced carbon atoms to certain materials. Fortunately,
246 carbon nanocontainers likely lose only a small fraction of their total carbon during
247 electron irradiation before their walls become instable and break up (Sun et al. 2006a),
248 and carbon is incompatible with most geophysically important minerals.

249 **APPLICATION TO EARTH SCIENCES**

250 We used pressurization during TEM to address a long-standing geochemical
251 question regarding the storage mode of carbon within mantle minerals (Wu and Buseck

2013). Using EFTEM, carbon concentrations of several atomic percent were detected along a stacking fault in titanium dioxide *in situ* at over 8 GPa and 770 °C (Fig. 10). Such measurement is impossible using other currently available high-pressure techniques. Thus, this procedure helped in the discovery of a new mechanism for hosting mantle carbon by segregation to crystal defects in an analog of a mantle mineral. This result has potential applications for geoscientists and others concerned with mantle geochemistry and geophysics, as well as with the deep carbon cycle.

IMPLICATIONS

High-pressure measurements in the earth and materials sciences have been expanded from DACs, MAPs, and shock experiments to include transmission electron microscopes using carbon nanocontainers as sample containers and presses. The advantage of the TEM approach is that dynamic changes can be observed in progress and, perhaps more importantly, materials can be examined at almost the atomic scale while at elevated pressure and temperature. The technique provides a new way of directly observing mineral structures and reactions at elevated conditions within an electron microscope, so that changes that occur deep within Earth or other planets can be studied in detail at high spatial resolution. Also, being able to observe materials in situ removes problems induced upon quenching if one wants to observe details of non-quenchable phases. Finally, determining the characteristics and properties of individual

nanograins using this technique can be extremely useful, whereas it is difficult with other methods currently available. A result is that the versatile power of TEM under ambient conditions that has long been familiar to earth scientists can now be extended to similar studies at elevated pressures and temperatures.

ACKNOWLEDGEMENTS

This work was financially supported by NSF grants EAR-0948535 and EAR-1148776. We acknowledge the use of facilities within the LeRoy Eyring Center for Solid State Science at Arizona State University. William Petuskey, Karl Weiss and David Wright are thanked for their technical assistance. We are also grateful to Ho-kwang Mao and an anonymous reviewer for their helpful comments.

REFERENCES CITED

Ajayan, P.M., and Iijima, S. (1993) Capillarity-induced filling of carbon nanotubes. Nature, 361, 333-334.

Akhtar, S., Rubino, S., and Leifer K. (2012) A simple TEM method for fast thickness characterization of suspended graphene flakes. arXiv:1210.2307.

Banhart, F. (1999) Irradiation effects in carbon nanostructures. Reports on Progress in Physics, 62, 1181-1221.

Banhart, F. (2004) Formation and transformation of carbon nanoparticles under electron irradiation. Philosophical Transactions: Mathematical, Physical and Engineering Sciences, 362, 2205-2222.

Banhart, F., and Ajayan, P.M. (1996) Carbon onions as nanoscopic pressure cells for diamond formation. Nature, 382, 433-435.

Buseck, P.R. (1992) Principles of transmission electron microscopy. Reviews in Mineralogy and Geochemistry, 27, 1-36.

Cordier, P. (2002) Dislocations and slip systems of mantle minerals. Reviews in Mineralogy and Geochemistry, 51, 137-179.

Cosslett, V.E. (1978) Radiation damage in high resolution electron microscopy of biological materials: A review. Journal of Microscopy, 113, 113-129.

Dujardin, E., Ebbesen, T.W., Hiura, H., and Tanigaki, K. (1994) Capillarity and wetting of carbon nanotubes. Science, 265, 1850-1852.

Karato, S. (2009) Rheology of the deep upper mantle and its implications for the preservation of the continental roots: A review. Tectonophysics, 481, 82-98.

Krasheninnikov, A.V., Banhart, F., Li, J.X., Foster, A.S., and Nieminen, R.M. (2005) Stability of carbon nanotubes under electron irradiation: Role of tube diameter and chirality. Physical Review B, 72, 125428.

Mao, H.K., and Hemley, R.J. (1998) New windows on the Earth's deep interior. Reviews in Mineralogy and Geochemistry, 37, 1-32.

Sanosh, K.P., Balakrishnan, A., Francis, L., and Kim, T.N. (2010) Sol-gel synthesis of forsterite nanopowders with narrow particle size distribution. Journal of Alloys and Compounds, 495, 113-115.

Smith, B.W., and Luzzi, D.E. (2001) Electron irradiation effects in single wall carbon nanotubes. Journal of Applied Physics, 90, 3509-3515.

Stixrude, L., and Lithgow-Bertelloni, C. (2012) Geophysics of chemical heterogeneity in the mantle. Annual Reviews of Earth and Planetary Sciences, 40, 569-595.

Sun, L., Banhart, F., Krasheninnikov, A.V., Rodríguez-Manzo, J.A., Terrones, M., and Ajayan P.M. (2006a) Carbon nanotubes as high-pressure cylinders and nanoextruders. Science, 312, 1199-1202.

Sun, L., Rodríguez-Manzo, J.A., and Banhart, F. (2006b) Elastic deformation of nanometer-sized metal crystals in graphitic shell. Applied Physics Letters, 89, 263104.

Tsang, S.C., Chen, Y.K., Harris, P.J.F., and Green, M.L.H. (1994) A simple chemical method of opening and filling carbon nanotubes. Nature, 372, 159-162.

Ugarte, D. (1992) Curling and closure of graphitic networks under electron-beam irradiation. Nature, 359, 707-709.

Veblen, D.R. (1985) Direct TEM imaging of complex structures and defects in silicates. Annual Reviews of Earth and Planetary Sciences, 13, 119-146.

Williams, D.B., and Carter, C.B. (1996) Transmission Electron Microscopy: A Textbook for Materials Science. Plenum Press, New York.

Wu, J., and Buseck, P.R. (2013) Carbon storage at defect sites in mantle mineral analogues. Nature Geoscience, 6, 875-878.

334 **TABLE 1.** Minerals placed into carbon nanocontainers and the methods used

335

Loading Methods		Loaded Minerals
Type-A containers	Capillary wetting by molten salts	molybdite (MoO_3), shcherbinaite (V_2O_5)
	Capillary introduction of soluble materials in solution, followed by annealing	magnetite (Fe_3O_4), bunsenite (NiO), zincite (ZnO), yttriaite (Y_2O_3), olivine (Mg_2SiO_4)
Type-B containers	Chemical vapor deposition with dispersed nanoparticles	olivine, anatase (TiO_2), rutile (TiO_2), barioperovskite ($BaTiO_3$), perovskite ($CaTiO_3$), tausonite ($SrTiO_3$)
	Laser ablation with suspended nanoparticles	olivine
	Arc discharge of target or precursor materials	cohenite (Fe_3C), iron (Fe), moissanite (SiC), naquite (FeSi)

336

337 **FIGURE 1.** Shrinkage of a carbon nanotube (CNT) that is caused by structural reorganization

338 around vacancies in its graphitic networks. (Adapted from Sun et al. 2006a)

339

340 **FIGURE 2.** Sketch of structures of some carbon nanocontainers. (**a**) CNT. (**b**) CNF. (**c**) CNO.

341

342 **FIGURE 3.** High-temperature synthesis apparatuses for producing carbon nanocontainers. (**a**)

343 Arc-discharge system and (**b**) tube-furnace assembly used for CVD and laser ablation. The

344 green light is from the laser beam. Both units were built at Arizona State University for growing

345 CNTs and CNOs.

346

347 **FIGURE 4.** Methods for loading carbon nanocontainers. (**a**) Magnetite (Fe_3O_4) nanocrystals
348 within a CNF. The mineral was placed into the CNFs by aqueous wetting in a $Fe(CH_3COO)_2$-
349 CH_3COOH solution followed by annealing in argon at 600 °C for 2 hours. The composition was
350 confirmed by the EELS spectrum, in which the oxygen and iron edges are indicated. (**b**)
351 Shcherbinaite (V_2O_5) nanocrystal within a CNT. The mineral was introduced into pre-opened
352 CNTs by capillarity from the molten state. The composition was confirmed by its EDS spectrum.
353 The C peak in this and other panels is from the CNT, and the Cu peak is from the TEM grid. (**c**)
354 Bunsenite (NiO) nanocrystal within a CNT. The mineral was placed into CNTs by aqueous
355 wetting in a $Ni(NO_3)_2$-HNO_3 solution followed by annealing in air at 500 °C for 2 hours. The
356 composition was confirmed by the EDS spectrum; the indicated fringe spacings match those of
357 bunsenite (111) and (020).

358

359 **FIGURE 5.** Forsterite (Mg_2SiO_4) nanocrystal within a CNF. Aqueous wetting of the CNF in a
360 $Si(OC_2H_5)_4$-$Mg(NO_3)_2$-HNO_3 solution was followed by annealing in air at 900 °C for 2 hours. The
361 composition was confirmed by the EDS spectrum. The C peak is from the CNT and the Cu peak
362 is from the TEM grid.

363

364 **FIGURE 6.** Time sequence of a cohenite (Fe_3C) nanocrystal in a contracting CNT. The panels
365 track changes occurring to the crystal during heating for 190 s at 500 °C, followed by an

366 essentially instantaneous increase to 800 °C. The morphology change of the cohenite crystal,
367 which resulted from surface-energy minimization of the carbide, occurred in less than 1 s.
368 Extended heating at that temperature resulted in additional CNT contraction and consequent
369 pressurizing of the encapsulated nanocrystal. There is a magnification increase between the two
370 panels at the bottom right. The images were recorded with a MEMS-based (Protochips Aduro)
371 heating holder within a Philips CM200 field-emission-gun electron microscope operated at 200
372 kV. The electron current densities were ~100-250 A/cm^2.
373

374 **FIGURE 7.** Compression series of an olivine nanocrystal subjected to non-hydrostatic stress in a
375 CNF at 410 °C. The compression directions are indicated by the increase in the vertical
376 dimension of the nanocrystal and decrease in its horizontal dimension. To minimize radiation
377 damage to the olivine, the electron beam was distorted into a thin band and then positioned
378 alternately along the outer edge of the CNF wall on opposite sides of the nanocrystal, as
379 illustrated by the blue dashed ellipses.
380

381 **FIGURE 8.** Radiation-induced compression of a zincite (ZnO) nanocrystal in a CNT at 500 °C. (**a**)
382 The crystal prior to irradiation. (**b**) Same crystal after irradiation for 5 minutes. (**c**)
383 Superimposition of FFTs from (**a**) in yellow and (**b**) in green. Compression is indicated by an
384 approximately 6% decrease in the (100) lattice spacing.

385

386 **FIGURE 9.** Compression sequence of an anatase nanocrystal enclosed within a CNO at (**a**) 0, (**b**)
387 10, (**c**) 13, (**d**) 26, (**e**) 40, (**f**) 43, (**g**) 54, and (**h**) 58 minutes after the start of electron irradiation. (**i**)
388 The Fourier-filtered image from the dashed region in (**h**) showing a stacking fault in the TiO_2.
389 Pressure was generated by shrinkage of the CNO at 770 °C (using ~30 A/cm^2 electrons).
390 Disappearance of anatase (101) planes and emergence of α-PbO_2-type TiO_2 (110) planes indicate
391 a phase transition between (**e**) and (**f**) (cf. insets). The stacking fault is indicated by a line
392 segment in (**h**) and an arrow in (**i**). (Adapted from Wu and Buseck 2013)

393

394 **FIGURE 10.** EFTEM images showing appreciable carbon signals at the location of the stacking
395 fault in the pressurized TiO_2 nanocrystal. The fault is illustrated in the upper inset. (**a**) Carbon
396 map. (**b**) Jump-ratio image. The yellow boxes highlight the faint carbon intensities. The line
397 profile in the lower inset shows the intensities integrated along the arrowed direction within the
398 box in (**a**), with the central peak representing the carbon signals along the stacking fault. (From
399 Wu and Buseck 2013)

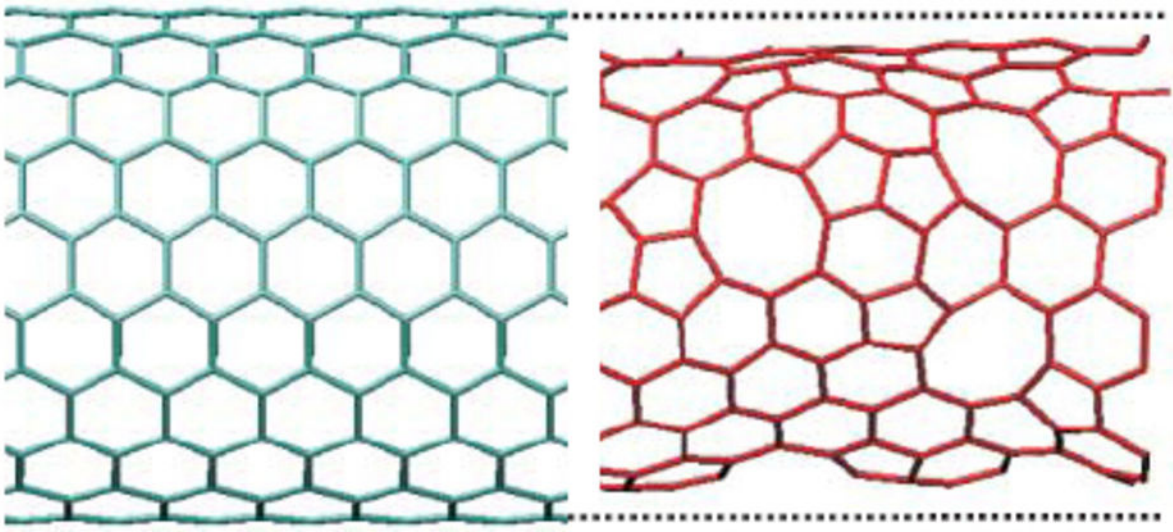

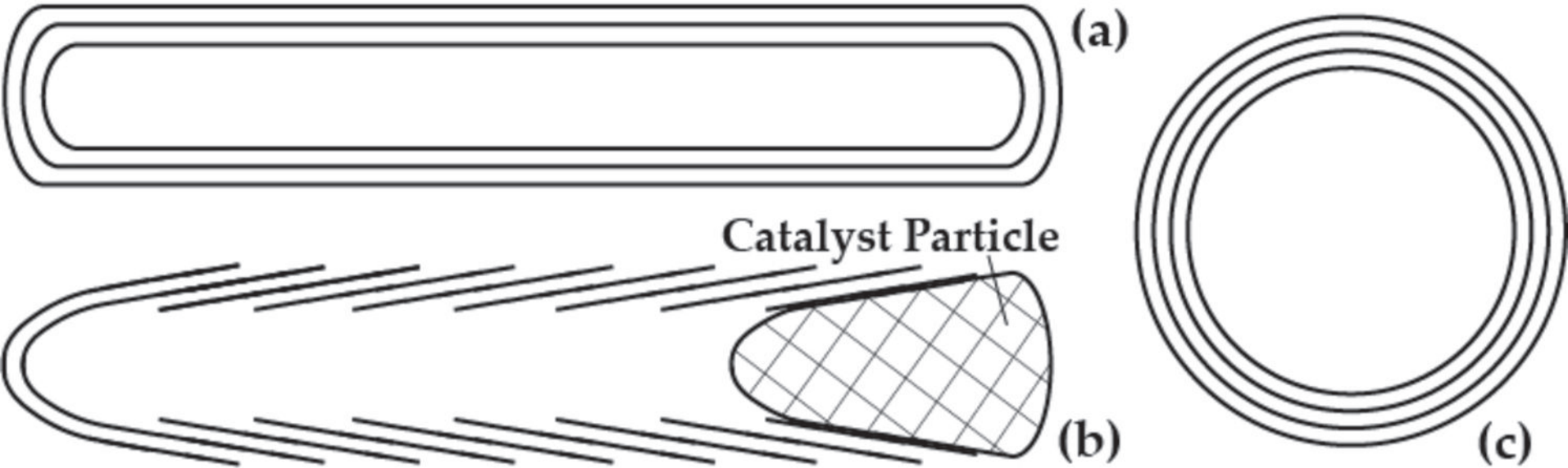
(a)
Catalyst Particle
(b)
(c)

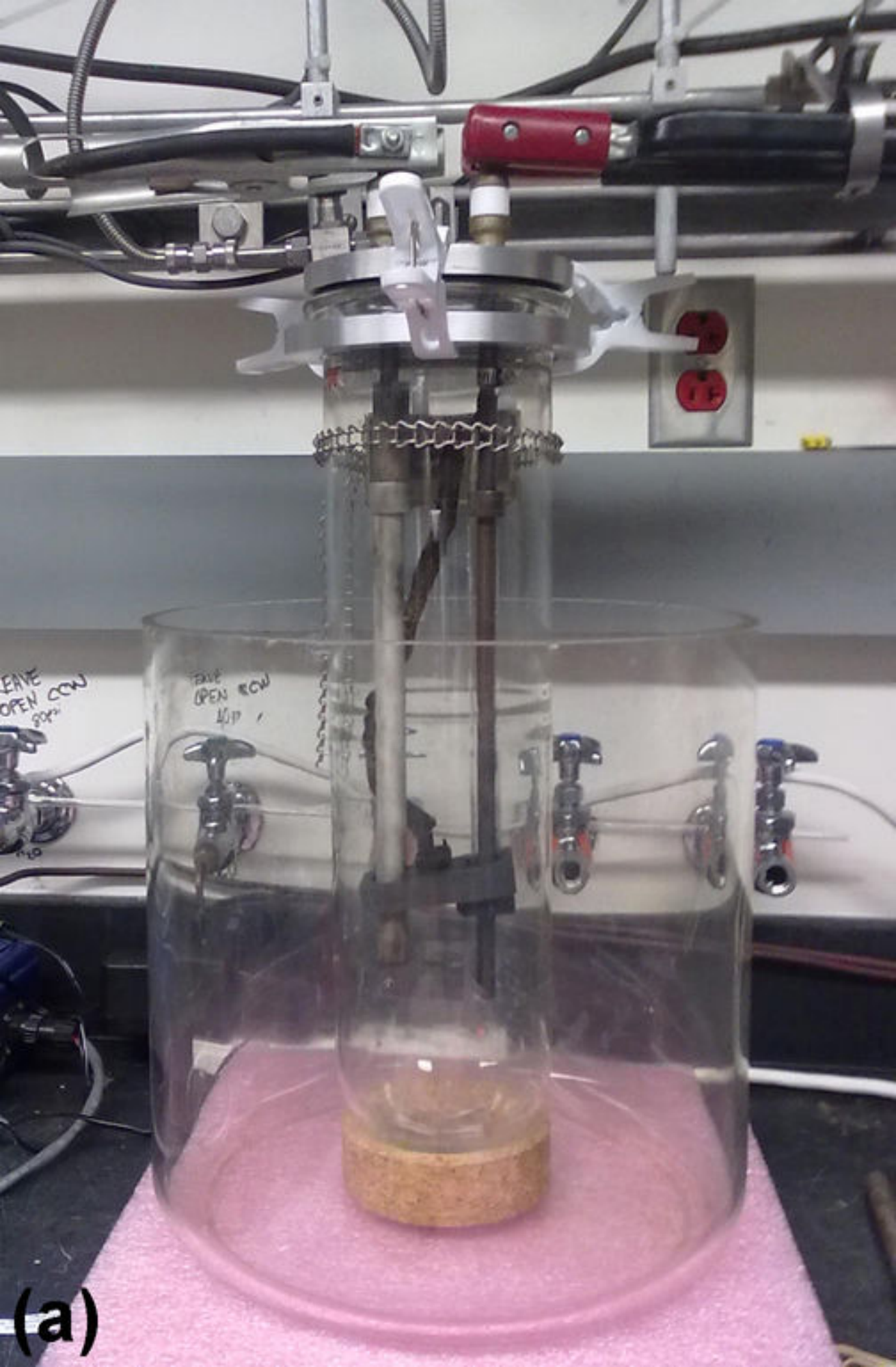
(a)

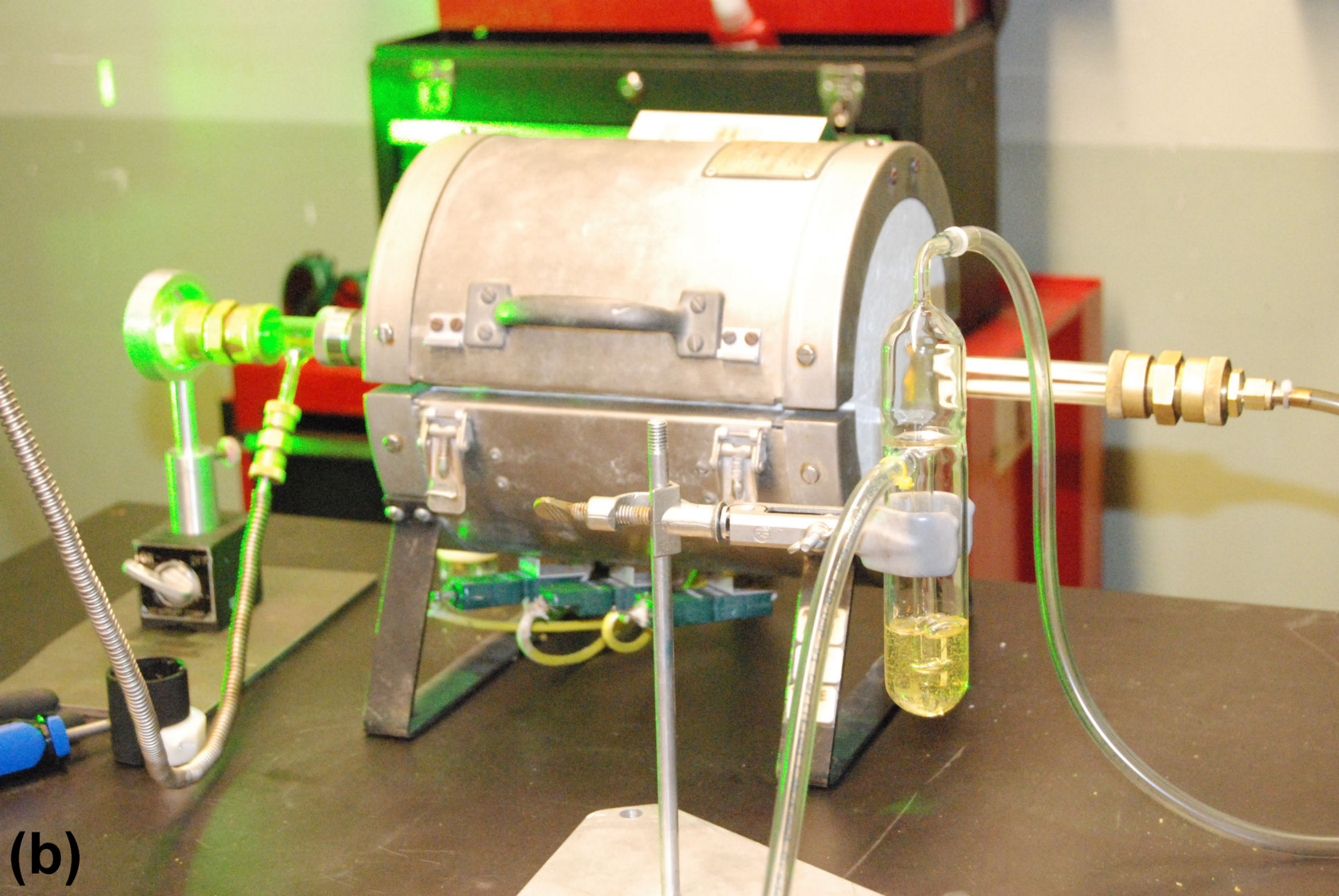
(b)

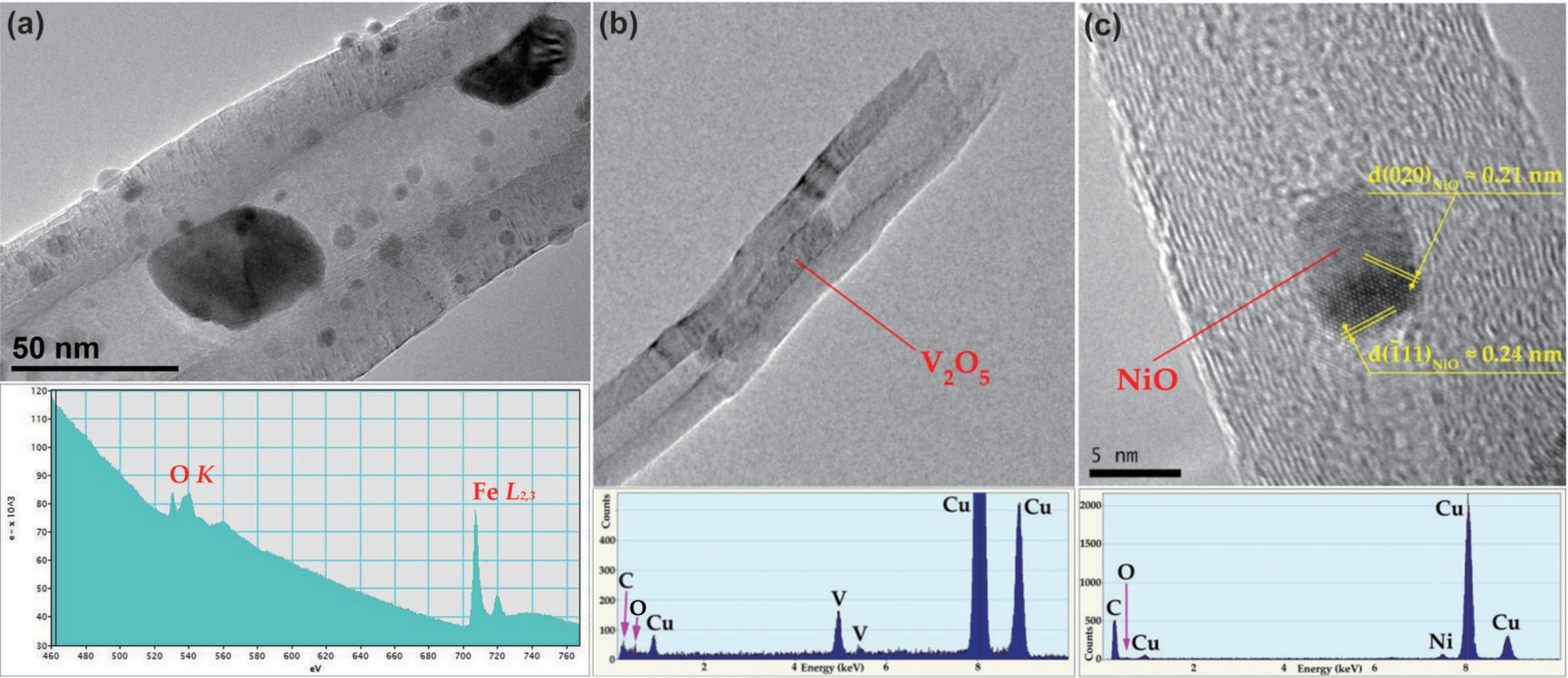
(a)
50 nm
(b)
V_2O_5
(c)
NiO
$d(020)_{NiO} \approx 0.21$ nm
$d(\bar{1}11)_{NiO} \approx 0.24$ nm
5 nm
O K
Fe $L_{2,3}$
e - x 10^3
eV
Counts
Energy (keV)
C
O
Cu
V
Ni

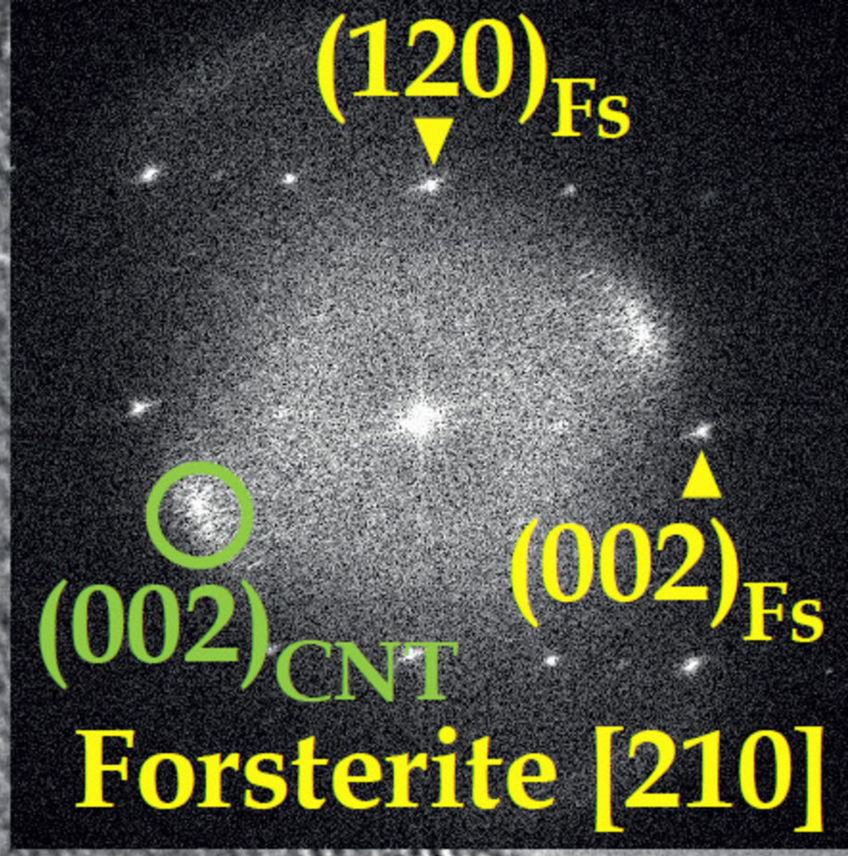
$(120)_{Fs}$
$(002)_{CNT}$
$(002)_{Fs}$
Forsterite [210]

10 nm

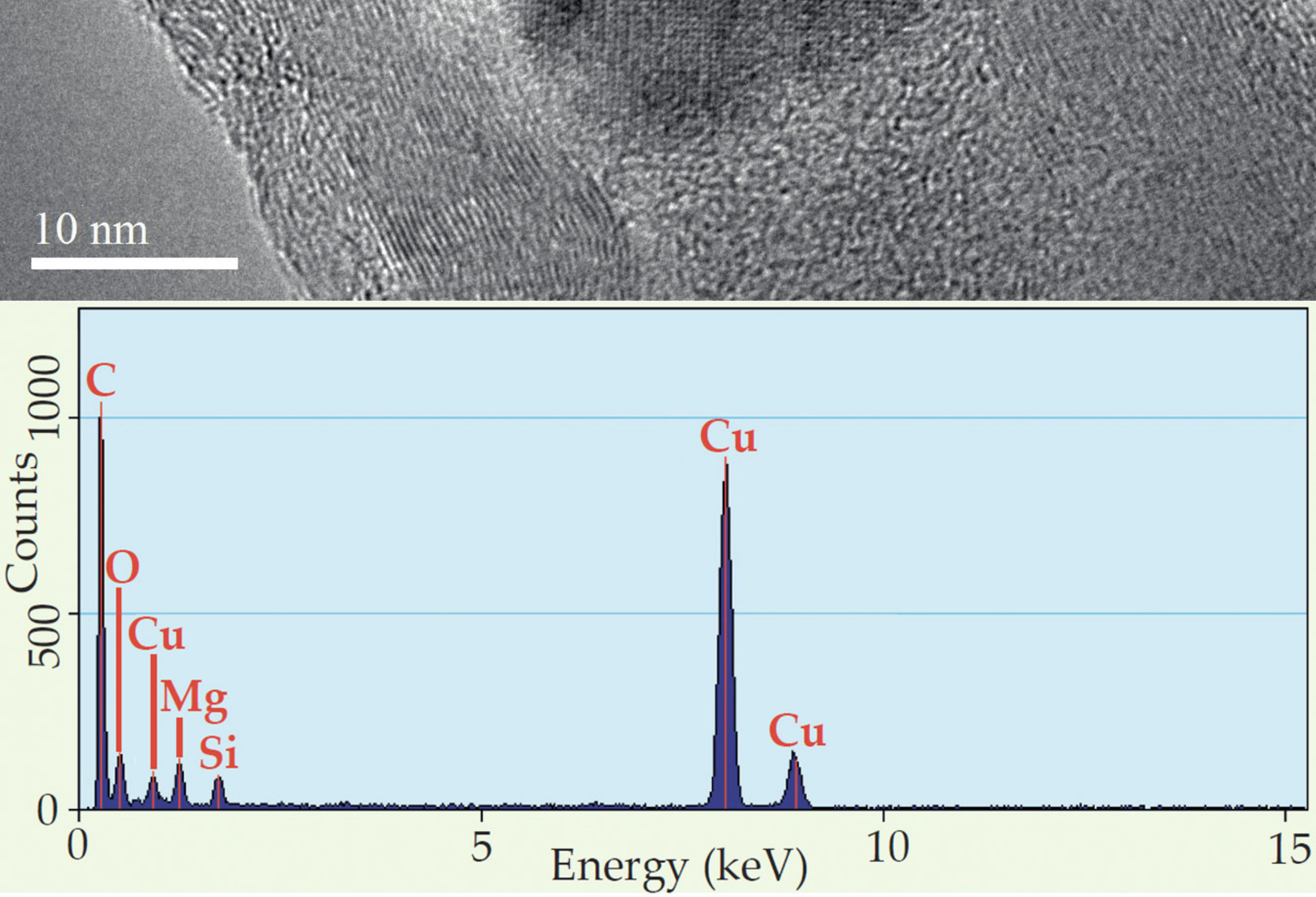
C
O
Cu
Mg
Si
Cu
Cu
Counts
0
500
1000
0
5
10
15
Energy (keV)

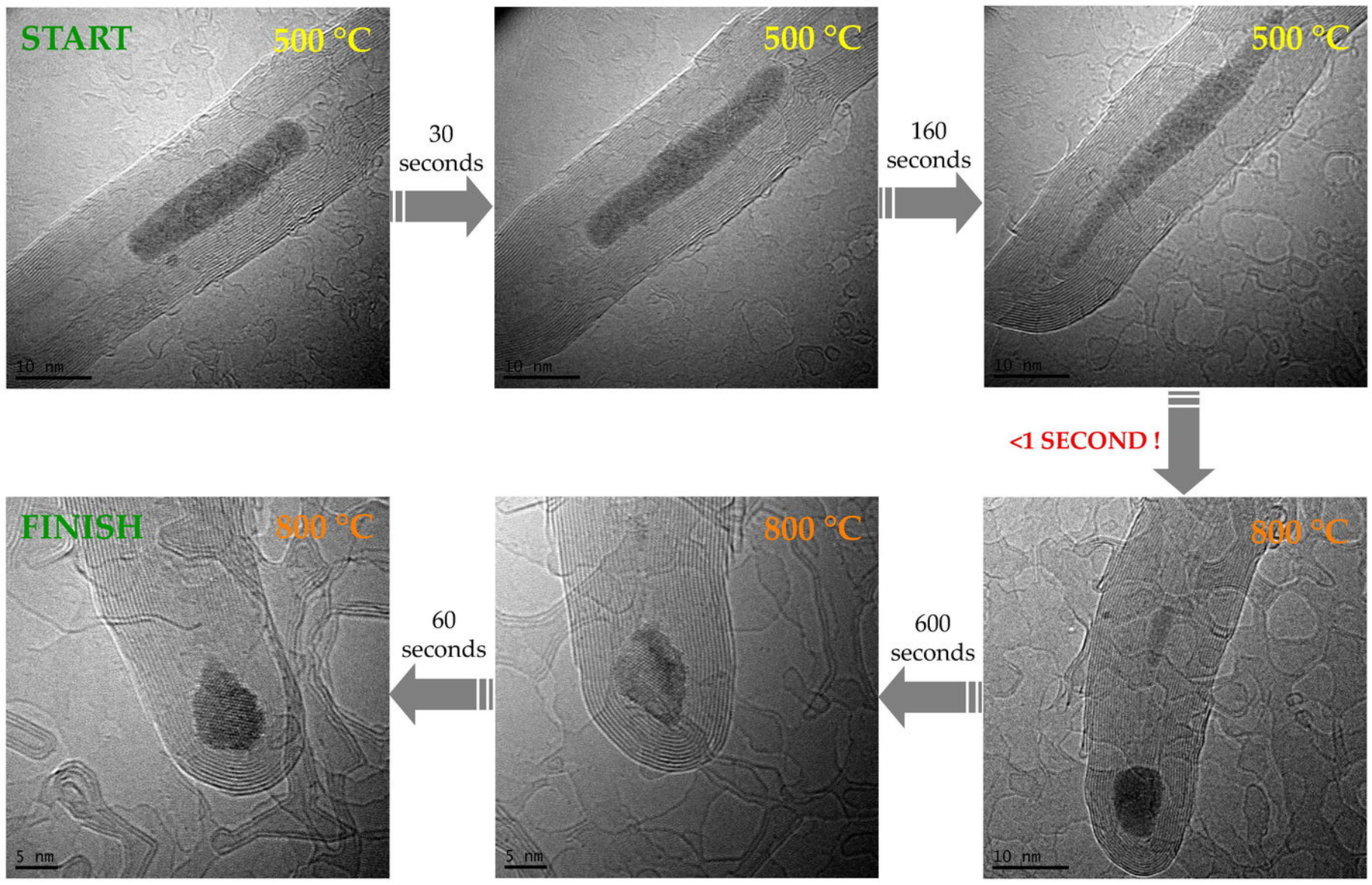
START
500 °C
10 nm
30
seconds
500 °C
10 nm
160
seconds
500 °C
10 nm
<1 SECOND !
800 °C
10 nm
600
seconds
800 °C
5 nm
60
seconds
FINISH
800 °C
5 nm

START

~66 nm

~85 nm

50 nm

17 min.

50 nm

59 min.

50 nm

100 min.

FINISH

~75 nm

~76 nm

50 nm

34 min.

50 nm

37 min.

50 nm

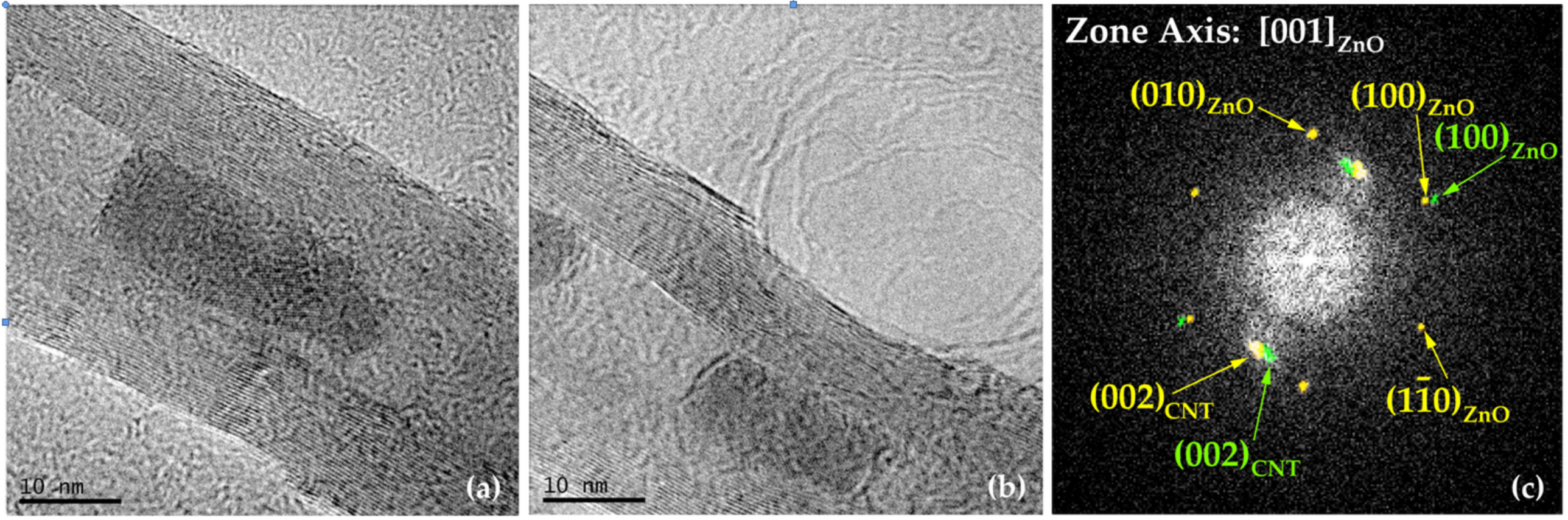
10 nm
(a)
10 nm
(b)
Zone Axis: [001]ZnO
(010)ZnO
(100)ZnO
(100)ZnO
(002)CNT
(002)CNT
(1$\bar{1}$0)ZnO
(c)

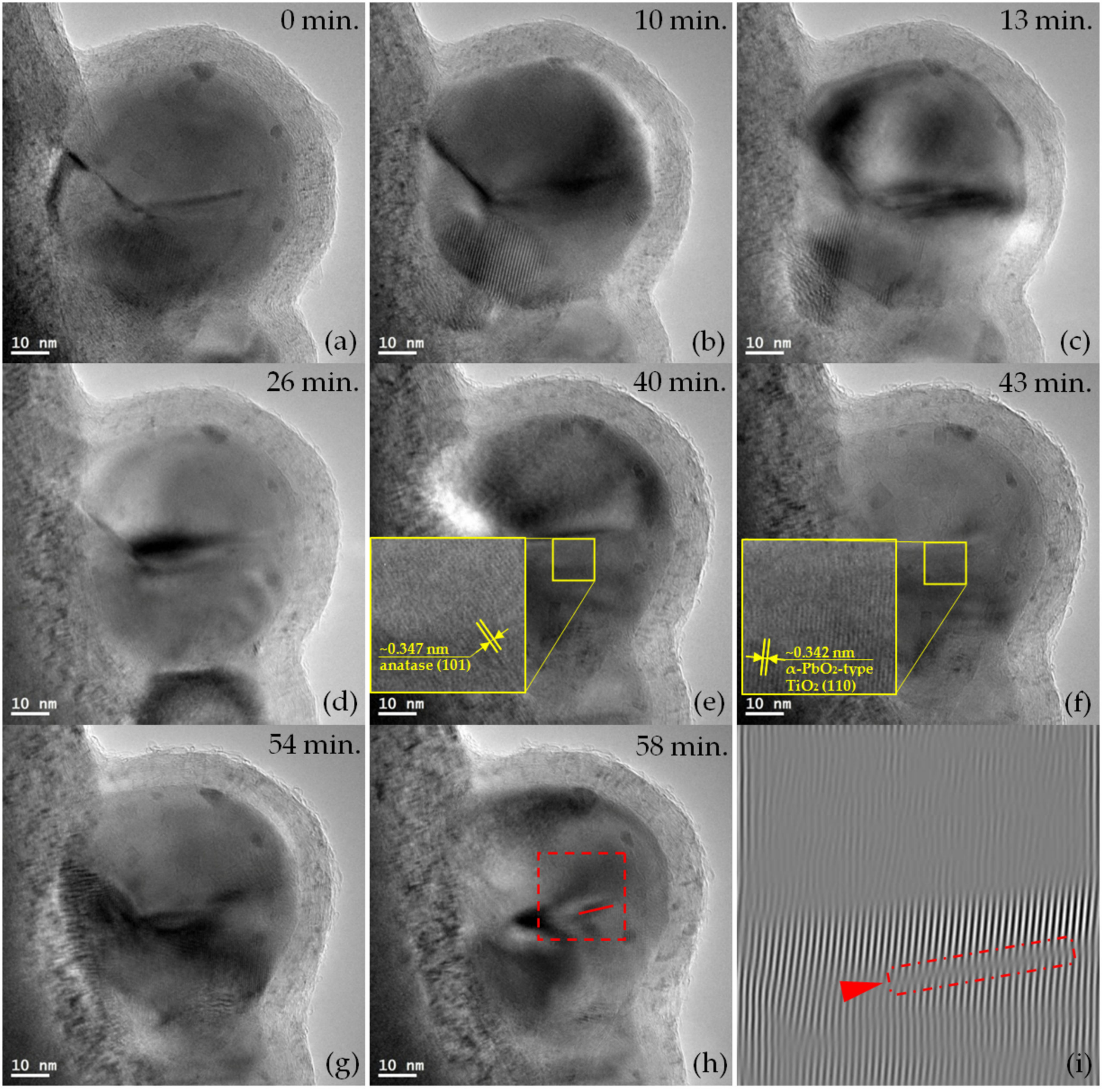
0 min.
10 nm
(a)
10 min.
10 nm
(b)
13 min.
10 nm
(c)
26 min.
10 nm
(d)
40 min.
~0.347 nm
anatase (101)
10 nm
(e)
43 min.
~0.342 nm
α-PbO2-type
TiO2 (110)
10 nm
(f)
54 min.
10 nm
(g)
58 min.
10 nm
(h)
(i)

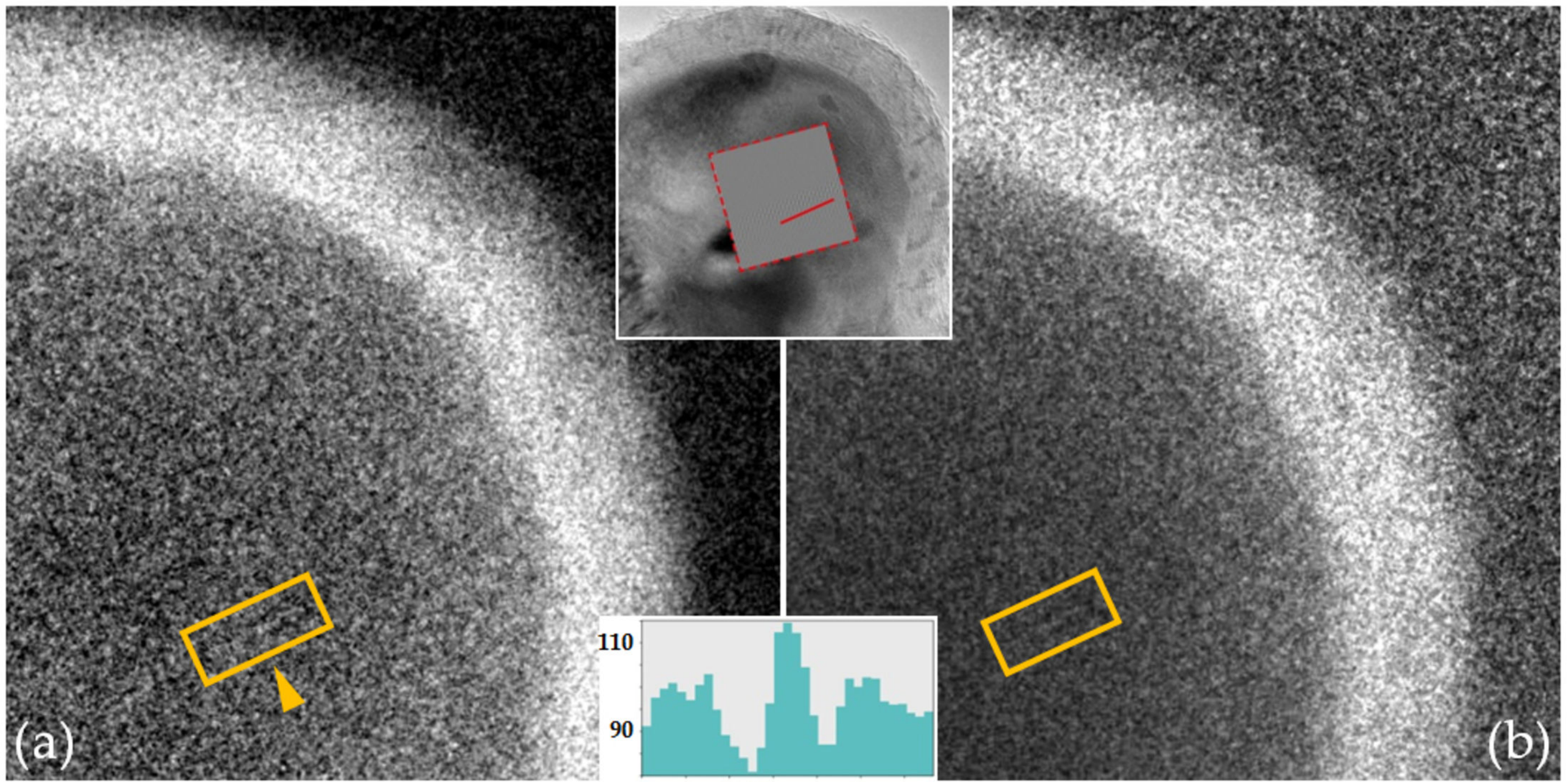
110
90
(a)
(b)